Importance of Hydrogen Migration in Catalytic Ammonia Synthesis over Yttrium-doped Barium Zirconate Supported Ruthenium Nanoparticles: Visualization of Proton Trap Sites

Christopher Foo[1,2†], Joshua Fellowes[1†], Huihuang Fang[1], Alexander Large,[2] Simson Wu,[1] Georg Held,[2] Elizabeth Raine[1], Ping-Luen Ho[1], Chiu Tang[2], and Shik Chi Edman Tsang[1]*

†Authors contributed equally to the work.as co-first authors.

[*]Corresponding author email: edman.tsang@chem.ox.ac.uk

[1]Wolfson Catalysis Centre, Department of Chemistry University of Oxford, Oxford, OX1 3QR, UK
[2]Diamond Light Source, Didcot, OX11 0DE, UK

Abstract

Barium zirconate perovskites have been systematically investigated as protonic supports for ruthenium nanoparticles in the Haber-Bosch ammonia synthesis reaction. A series of supports based on barium zirconate were synthesised, for which the B-site of the ABO_3 perovskite was doped with different aliovalent acceptor cations and in varying ratios, resulting in varying proton conductivities and trapping behaviours. Crucially, we provide direct evidence of the importance of a hydrogen-migration mechanism for ammonia synthesis over these proton-conducting materials from the studies of reaction kinetics, in-situ XPS and neutron powder diffraction (NPD), which requires the proper balance of oxygen vacancy concentration (B-site doping), trapping-site concentration, and proton-hopping activation energy. We report evidence of a large dynamic coverage of OH groups on the support and the first visualization of both weak and strong proton trap sites within the perovskite lattice through the use of NPD.

Introduction

The Haber-Bosch (HB) process was discovered in 1913[1], and is still the dominant production method for ammonia. As of 2020, annual global production exceeds 146 million tons[2], 88% of which is used in the production of agricultural fertiliser[2]. The subsequent increase in the availability of fertilisers facilitated the rapid increase in human population in the early 20th century[3], making the HB process one of the most important and well-established industrial chemical processes.

In addition to the current demand, ammonia is expected to hold future importance due to declining dependence on fossil fuels, through the development of sustainable energy storage. Although the energy density of ammonia is lower than liquid hydrocarbons (ammonia at 10 bar: 13.6 GJ m^{-3} vs. gasoline, C_8H_{18} at 1 bar: 34.4 GJ m^{-3})[4], ammonia possesses many advantages over conventional fossil fuels. Ammonia releases no carbon on combustion and can be sustainably produced by a variety of electrical and thermal processes from syngas or water splitting[5,6]. Liquidised ammonia also possesses advantages over hydrogen gas, in its increased energy density (13.6 GJ m^{-3} at 10 bar vs. 3.6 GJ m^{-3} at 14 bar, metal hydride storage system[4]), as well as its increased safety and ease of transport.

However, the HB remains a kinetically challenging reaction to achieve because it is highly energetically unfavourable to overcome the high dissociation energy of $N\equiv N$ (945 kJ mol^{-1})[7]. In addition, from thermodynamic viewpoint, it is also a highly energy-intensive process considering the huge energy is consumed for hydrogen synthesis (via syngas) prior to the ammonia production. Mittasch's catalyst is an iron catalyst with a potassium promoter[8,9]. Though it is considered a benchmark for ammonia synthesis and has remained largely unchanged for many decades, the required temperature and pressure are very high, making the process highly energy intensive for a large scale operation (400-500°C, 150-300 bar)[10]. A much milder process in using the intermittent renewables (solar, wind and tidal waves) is required in order to reduce our negative impact on the environment.

In the traditional HB reaction, the rate-determining step is known to be the dissociative adsorption of dinitrogen, resulting in surface-bound nitrogen adatoms, which subsequently undergo reaction with other adsorbed species by a Langmuir-Hinshelwood mechanism[11]. This barrier can be lowered by use of a catalyst by back-donation from the catalyst surface into the dinitrogen 2p π^* orbitals[12], for example, osmium, uranium, ruthenium, or cobalt-molybdenum[13]. Recent catalyst research has revealed a volcano-plot dependence of activity on d-electron count, and shown that ruthenium is the most active pure-metal catalyst[14].

The dissociation of dinitrogen over ruthenium metal has been found to be most favourable at step sites in which five ruthenium atoms are involved; these sites are referred to as B5 sites[15]. These sites bind dinitrogen more strongly and with a lower activation energy than terrace sites, as well as binding hydrogen relatively weakly[16]. The concentration of B5 sites is maximised for nanoparticles of approximately 2 nm in diameter. Below this size it is rare for the clusters to form the required shape, whereas above this size the bulk (0001) surface dominates[17–19]. Additional to the morphology of the nanoparticles, precursors that contain chlorine are prone to poisoning the catalyst surface due to strongly bound chlorine adatoms, which reduce the number of available catalytic sites and also reduce the dissociative ability of the metal surface by receiving electron density from the metal[20].

Inversely, electron transfer to the metal is known to promote the ability of the metal to dissociate dinitrogen, known as electronic promotion. Additional metal electron density has been shown to be beneficial by electron transfer from various sources (catalytic-activity dependent property in brackets): alkali metal ion dopants, known as promoters[6,17,21,22] (electropositivity); alumina-silicate zeolite supports[23,24] (basicity of framework oxygen atoms); electride materials[25] (concentration of extra-framework electrons). The additional electron density can be sourced from a reduced support, such as lanthanide oxides as first reported by Niwa and Aika[26]. Wang et al.[27] further showed that the high concentration of strong basic sites (30.5 μmol m^{-2}) in barium zirconate promotes ammonia synthesis. This report aims to build on this work by using caesium-promoted yttrium-doped barium zirconate supports.

The activation energy for the dissociation of dinitrogen can be reduced by increasing the strength of binding for nitrogen adatoms, making the rate-determining step the hydrogenation of nitrogen adatoms.

However, in general it is problematic to increase the strength of adatom binding, since this increases the binding of reaction intermediates (namely -H, -N, and -NH), which retards ammonia synthesis. This scaling relation can be avoided by changing the pathway of the reaction, for example by forcing an associative adsorption of dinitrogen[28] or facile hydrogenation via a $LiNH_2$ intermediate as opposed to nitrogen adatoms[29]. This stepwise mechanism for hydrogenation of absorbed N_2 to ammonia without the initial N_2 dissociation (associative process) over these catalysts is particularly attractive since it may catalyse the reaction at milder conditions[28].

Specifically, after the homolytic splitting of dihydrogen ($2\ Ru + H_2 \rightarrow 2\ Ru\text{-}H^0$), an excessive surface coverage of hydrogen adatoms leads to significant reduction in activity, commonly accompanied by a highly negative reaction order for dihydrogen (~-1)[6,21,28,30]. Such hydrogen poisoning at B5 active sites can be alleviated by the use of supports that can transport hydrogen species away from the catalyst surface by reversibly accommodating hydrogen species in a loosely bound state, for example hydride in electrides[25] or doped perovskite oxides as presented here, or by moving hydrogen across the catalyst surface through the use of electric fields[31].

Hence, it is an important area of research to (1) increase the electron density at the ruthenium surface for dinitrogen dissociation while maintaining relatively weak intermediate binding, and (2) increase the transport of hydrogen adatoms away from the metal catalyst surface by a protonic support. These criteria are fulfilled by using aliovalent-doped rare-earth oxide supports with alkali metal promoters.

We propose that hydrogen adatoms that poison the ruthenium surface can react with the oxide support to form surface lattice hydroxyl species. As well as alleviating hydrogen poisoning, which allows the continued adsorption of nitrogen and hydrogen, the surface lattice protons can be transferred and can also react with nitrogen adatoms to proceed the reaction at different locations (Equation 1). Accompanying this proton abstraction is the liberation of an electron into the ruthenium conduction band. The higher energy state facilitates stronger back-bonding during the dissociation of nitrogen, accelerating the rate-determining step of the Haber-Bosch reaction. Hence, the hydrogen spill-over mechanism from the ruthenium metal catalyst to the oxide support with oxygen vacancies not only provides a reversible and labile hydrogen store (hydrogen poisoning alleviation), but also enhances the dissociating ability of the metal (electronic promotion) under dynamic conditions. It is therefore important to provide further understanding how the nature of the oxide support accepts hydrogen from the ruthenium metal catalyst.

$$(a) \quad \mathrm{Ru(H^{\times})} + \mathrm{O_o^{\times}} \rightarrow \mathrm{Ru(e')} + \mathrm{OH_O^{\bullet}}$$

$$(b) \quad \mathrm{Ru(N^{0})} + \mathrm{OH_O^{\bullet}} + \mathrm{Ru(e')} \rightarrow \mathrm{Ru(NH^{0})} + \mathrm{O_o^{\times}} + \mathrm{Ru(e')}$$

Equation 1. Kroger-Vink notation of hydrogen spill-over mechanism. (a) Hydrogen abstraction by lattice oxides; (b) hydrogenation of nitrogen adatoms by hydrogen stored as lattice hydroxyl.

$$\text{(a)} \quad Zr_{Zr}^{\times} + Y^{3+} + 2\,O_O^{\times} \rightarrow Y_{Zr}' + 2\,V_o^{\bullet\bullet} + ZrO_2$$

$$\text{(b)} \quad \mathrm{H_2O_{(g)}} + \mathrm{V_O^{\bullet\bullet}} + \mathrm{O_o^{\times}} \rightarrow 2\,\mathrm{OH_O^{\bullet}} \qquad \text{(c)} \quad \mathrm{H_2O_{(g)}} + 2\,\mathrm{O_o^{\times}} + \mathrm{V_O^{\times}} \rightarrow 2\,\mathrm{OH_O^{\bullet}} + \mathrm{O_V''}$$

Equation 2. Kroger-Vink notation of formation reactions of proton-transport dependent lattice hydroxyl species: (a) Oxygen vacancy formation by reaction of aliovalent doped yttrium; (b-c) lattice hydroxyl formation by reaction of water with (b) oxygen vacancies[26], and (c) structural defects[32].

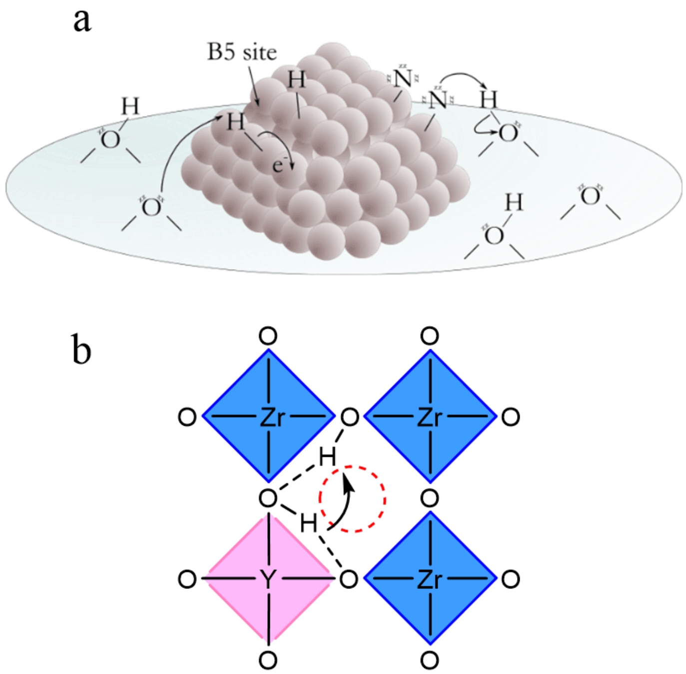

Scheme 1. (a) Proposed mechanism for reversible hydrogen spill-over from poisoned ruthenium catalysts to BZY perovskite supports. (b) Proton dynamics in BZY lattice, modified from Yamazaki et al.[33]: motion of proton between YO_6 and ZrO_6 octahedra showing a spatial rearrangement of proton with the proton trap escape mechanism; octahedral hole shown in red.

Proton conduction in ceramics at elevated temperatures was first confirmed by Iwahara et al. in 1981 for a ytterbium-doped $SrCeO_3$ perovskite during water splitting[34]. Barium cerates, $BaCeO_3$ (BC), and zirconates, $BaZrO_3$ (BZ) are the most researched protonic ceramics due to their high proton conductivities. BZ in particular exhibits excellent stability against H_2O, CO_2, and H_2S, and significant bulk proton conductivities at high temperatures (300-600°C)[35–39]. (Only moderate proton conduction is observed at temperatures below 100°C.) However, the total proton conductivities of BZ are notably not as high as BC due to grain boundary resistance, which is attributed to reactant impurities and the required high sintering temperatures[32,40]. As a support for ruthenium nanoparticles, it has been shown to exhibit the highest rate of ammonia synthesis amongst a range of supports[26,27].

For these protonic perovskites it is well-known that surface lattice hydroxyl species $(\mathrm{OH}_\mathrm{O}^{\bullet})$ can be formed initially through reversible water activation by lattice oxygen vacancies (Equation 2). The proton transport properties have been shown to be a function of oxygen vacancies or resulting concentration of $\mathrm{OH}_{\mathrm{O}}^{\bullet}$ surface coverage to offer proton hopping to take place. Water can also fill neutral oxygen vacancies, which are known as structural defects as opposed to electronic defects.

While BZ does have intrinsic oxygen vacancies, the concentration can be significantly increased by partial occupation of the tetravalent B-site (Zr^{4+}) with aliovalent trivalent rare-earth cations (Ce^{3+}, Y^{3+}, Yb^{3+}, Er^{3+}, etc.) by adapting stoichiometry during synthesis, $BaZr_{1-x}M_xO_3$. The acceptor dopant, $\mathrm{M}_{\mathrm{Zr}}'$, establishes a charge imbalance that induces extrinsic oxygen vacancy defects, thereby increasing proton conductivity[41] with the dynamic coverage of surface OH (Scheme 1). This report will focus on yttrium-doped BZ (BZY*x*, *x* = %mol B-site occupancy by yttrium), in which it has previously been shown that both total and grain-boundary proton conductivity peak at 10-20%mol before a significant decrease at lower or higher doping levels[40]. However, they offered no rationalization for the optimum yttrium-doping level. We propose that the highly doped oxides suffer from strong proton traps at the aliovalent B-site ($\mathrm{OH}_{\mathrm{O}}^{\bullet}$-$\mathrm{M}_{\mathrm{Zr}}'$), which hinder proton conduction.

The mechanism for protonic conduction has been much investigated. Firstly, the Grotthuss mechanism[42–46] in which protons are classically transported to neighbouring oxygen sites (both intra- and inter-polyhedral[47,48]); this is in contrast with the vehicle mechanism in which the hydroxyl species moves as a whole. Additionally, a phonon-assisted mechanism has been shown in which the proton-phonon interaction is manifest as a Holstein polaron[49] (or small polaron, defined as such when a polaron's range of interaction is shorter than the unit cell); this induces movement of the neighbouring hydroxyl groups, which are otherwise considered static. Recently, Yamazaki et al.[37] reported the proton dynamics in BZY structure from their DFT calculation (Scheme 1). They showed that a spatial rearrangement of proton from a deep trap site (shared Y^{3+}/Zr^{4+} octahedra) to move along the ZrO_6 octahedra (shallow trap sites) probably via interstitial sites before forming a new hydrogen bond attached to a ZrO_6 octahedra. However, further experimental identification of these proton sites is yet to be confirmed.

Here, we report on the correlation of ammonia synthesis performance of ruthenium nanoparticles with proton conductivity and structural aspects of a series of rare-earth doped barium zirconate materials in systematic manner. In particular, we aim to experimentally elucidate the importance of hydrogen migration in this catalysis reaction using in-situ XPS and neutron diffraction with the identification of the weak and strong proton trap sites.

Methods

Synthesis of Barium Zirconate

Yttrium-doped BZ supports were synthesised by a citrate-EDTA (ethylenediaminetetraacetic acid) complexation method. Yttrium nitrate hexahydrate ($Y(NO_3)_3 \cdot 6H_2O$), barium nitrate ($Ba(NO_3)_2$), and zirconium oxynitrate hydrate ($ZrO(NO_3)_2 \cdot xH_2O$) (Sigma Aldrich) were used as reagents. Hydration of zirconium oxynitrate was determined by TGA analysis, with x between 2 and 2.5.

In a typical procedure, $BaZr_{1-x}Y_xO_{3-\delta}$ was synthesised by dissolving the metal nitrate salts in water in stoichiometric ratios under high stirring. Relative to the metal ion stoichiometry, 1.5 eq. of both EDTA and citric acid were added. After each addition, the pH was adjusted to ~10 using aqueous ammonium hydroxide. The solution was heated in an oven until combustion. The resulting ash was crushed into a fine powder and calcined in a furnace under high airflow at 1300°C for 4 hours, yielding an off-white powder. Complete calcination was confirmed by powder XRD. This procedure was repeated with adapted stoichiometry to synthesise rare-earth-doped materials, $BaZr_{0.8}M_{0.2}O_{3-\delta}$, M = Er, Ho, Y, Yb, as well as yttrium-doped perovskites with increasing degrees of doping, $BaZr_{1-x}Y_xO_{3-\delta}$, where $x = 0, 0.1, 0.2$, and 0.5. The powders were then wet-milled using iso-propanol (Fritsch P7, zirconia, 1 mm balls) milled at 500 rpm in six cycles of 5 minutes with a 3-minute rest to dissipate excess heat (total milling time of 30 minutes).

Supporting Ruthenium Nanoparticles on Barium Zirconate

Both ruthenium(III) acetylacetonate ($Ru(acac)_3$) and tri-ruthenium dodeca-carbonyl ($Ru_3(CO)_{12}$) precursors were investigated. Ruthenium nanoparticles were synthesised by wet impregnation, followed by temperature controlled chemical vapour deposition reduction. Typically, 100 mg Ru(acac)$_3$ was dissolved in 1 mL acetone, and sonicated with the support material for 2 hours, then stirred overnight and dried in an oven for 2 hours to yield a red powder. The powder was reduced in a furnace under 30 mL min^{-1} 5% H_2:Ar flow, heated to 150°C, held for 24 hours, then to 350°C, held for 24 hours, and cooled to room temperature. A ramp rate of 5°C min^{-1} was used. The catalyst was passivated for 2 hours under 30 mL min^{-1} 2.5% O_2: He to yield a grey powder.

Catalyst formation from $Ru_3(CO)_{12}$ was carried out according to Aika et al.[20]. $Ru_3(CO)_{12}$ was dissolved in tetrahydrofuran (20 mL per 30 mg $Ru_3(CO)_{12}$), to give an orange solution. The support material was added to result in a 15%wt ruthenium loading. The high Ru content was mainly chosen due to facilitated characterization (i.e. TEM, XPS) but optimization in Ru size and dispersion for optimized catalysis are not yet performed.

The resulting suspension was sonicated for 6 hours, then separated by rotary evaporation, yielding an orange powder. De-carboxylation of $Ru_3(CO)_{12}$ was carried out to yield supported ruthenium nanoparticles. The orange powder was heated in a furnace under 50 mL min^{-1} argon to 70°C, held for 4 hours, then to 350°C, held for 5 hours, and cooled to room temperature. A ramp rate of 2°C min^{-1} was used. A grey powder was obtained, typically with yields greater than 90%. No passivation was employed for this preparation.

Addition of a Caesium Promoter

Caesium promoters were added to the catalysts using wet impregnation. Caesium nitrate ($CsNO_3$) was dissolved in the minimum volume of water (2–3 mL for 200 mg) under stirring. The catalyst was added to yield 5%wt loading. The thick slurry was stirred for 5 hours, before drying in a vacuum oven at 70°C overnight. The $CsNO_3$ was reduced in-situ prior to testing; reports suggest it is reduced to sub-symmetric oxide, Cs_xO_y, $x/y = 2.7–3.7$.

Catalytic Testing

Catalysts were tested in a tubular fixed-bed reactor. Typically, 100 mg of catalyst was loaded into a quartz tube and secured using quartz wool. Before testing, surface oxide on the ruthenium nanoparticles was reduced under 50 mL min^{-1} H_2 flow at 450°C.

For the range of rare-earth doped catalysts derived from $Ru(acac)_2$, the reactor was heated to 450°C and pressurised to 50 bar using 50 mL min^{-1} flow of 3:1 H_2:N_2. For the kinetic study of Cs-RuBZY derived from $Ru_3(CO)_{12}$, temperatures between 350°C and 450°C were used for hydrogen partial pressures between 1.25 bar and 7.5 bar. A constant partial pressure of nitrogen of 2.5 bar was used and made up to a total pressure of 10 bar by adding argon. A high flow rate of 200 mL min^{-1} was used to ensure the reaction took place far from the equilibrium.

For both investigations, the reaction was allowed to stabilise under pressure and flow for 1 hour before measurements were taken. The rate was determined by bubbling exhaust gases through an acid trap of known volume (10 mM H_2SO_4). The concentration of the trap was measured by an ammonium ion-selective electrode.

Synchrotron Powder XRD

Diffraction data was collected from samples BZY, BZY10, BZY20, and BZY50 at BL02B2, SPring-8, Japan[50]. Samples were loaded into borosilicate capillaries of diameter 0.5 mm, and analysed by Debye-Sherrer geometry using a position-sensitive MYTHEN detector over an angular range of 4–78° in 2θ over a 10-min exposure period (sum of 2 × 5 min) under atmospheric conditions. The beam energy was shown to be 0.6885110(3) Å (18.007591 keV) by refinement of a ceria standard. The angular zero-error of the sample environment and diffractometer was refined to be −0.00134(1)°.

Neutron Powder Diffraction

Time-of-flight neutron powder diffraction data was collected at the Swiss Spallation Neutron Source (SINQ) at the Paul Scherrer Institute, Switzerland. The diffraction parameters are as follows: flight length: 42.2992 m, detector angle in two-theta: 121.660°. Catalysts were prepared using the typical synthesis procedure. For each measurement, 3 g of sample were reduced at 450°C, under 50 mL min^{-1} 5% H_2/Ar flow. The gas was then switched to an argon line passed through a bubbler filled with D_2O without exposing the catalysts to ambient atmosphere. After reduction, each sample was heated to 600°C under Ar, either dry or D_2O saturated. Samples were then sealed in Schlenk tubes in a glove box and measured immediately in order to limit exchange with atmospheric water. Data was collected at ambient temperature.

In-situ near-ambient pressure XPS

Prior to testing, all samples were in situ reduced under 1 bar hydrogen at 450°C for 2 hours. High resolution data was collected at 720 eV and 900 eV to observe changes in the Ru 3d and O 1s band, respectively.

Spectra were collected under ~40 mbar H_2, then ~10 mbar Ar, and finally again under ~40 mbar H_2 under the same reaction temperature. The pressure is inversely proportionate with X-ray transparency[51]; hence spectra collected under 10 mbar argon are much more intense than under 40 mbar H_2 due to much higher photo-electron flux at the detector (electron total-scattering cross-section at 50 eV[52,53]; H_2: 2.625 a_0^2, Ar: 30.464 a_0^2). Therefore, hydrogen can be used at higher pressures. It was decided to use the highest possible pressures for each gas in order to enhance the effect of changing atmosphere.

For ruthenium signals, the Ru 3d peak is split into two spin-orbit coupled peaks from the Ru $3d_{5/2}$ and Ru $3d_{3/2}$ bands, with bandgap 4.17 eV, and area ratio of 3:261. The presence of satellite peaks was observed, likely from trace ruthenium oxide or carbonate on the surface. The Ru 3d photoemission region strongly overlaps with the C 1s region, meaning the Ru $3d_{3/2}$ peak is not directly observable; hence changes in binding energy were quantified using only the Ru $3d_{5/2}$ peak. The carbon peaks were modelled using three separate sources of carbon photoemission: adventitious or graphitic carbon (C-C and C-H bonds), alcohol species, and carbonate species. Ruthenium and carbon peaks were modelled with asymmetric Lorentzian functions. Spectra were modelled using Casa XPS software. Shirley backgrounds were used for all regions, and two 5-point moving-average smoothing operations were applied.

Results and discussion

Varying rare-earth dopant

Rare-earth-doped BZ materials were synthesised which have been shown by Han et al.[54] to exhibit the most favourable properties (total electronic conductivity, proton concentration, and proton-induced lattice distortion), $BaZr_{0.8}M_{0.2}O_{3-\delta}$, M = Er, Ho, Y, Yb. The XRD patterns for all materials confirmed the formation of the cubic *Pm-3m* barium zirconate structure by comparison to a theoretical pattern (Figure 1). The doped materials have slightly broader peaks than non-doped BZ, which is attributed to smaller crystallite size. TEM micrographs show that the particles are several hundred nanometers in diameter and exhibit a degree of porosity (Figure S1). This can be explained through increased micro-strain due to mixed B-site occupancy and decreased crystallinity leading to hindered nucleation. Lattice parameters yielded by Pawley refinement show that the doped perovskites have enlarged unit cells (Figure S2 and S3). The deviation in lattice parameter from BZ (4.196 Å) is not proportionate with the known ionic radii of the eight-fold coordinated trivalent rare-earth-element ions, which indicates additional electronic interactions and structural distortions that are unaccounted for.

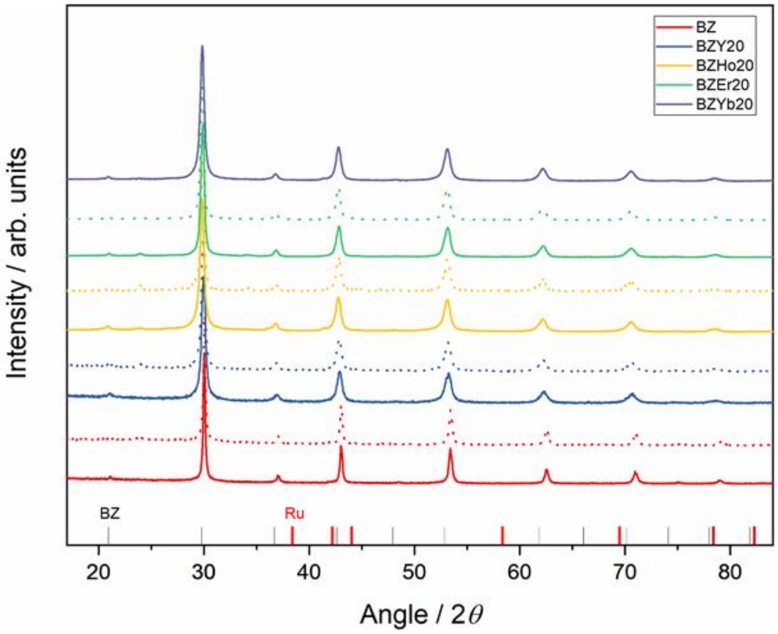

Figure 1. XRD patterns of rare-earth-doped supports before (solid) and after (dotted) ruthenium loading and reduction. Simulated powder diffraction patterns for BZ (solid) and Ru (dotted) shown.

After ruthenium dispersion and reduction, the structures of the pristine supports are shown to be retained with similar crystallinities (Figures S2 and S3). There are also no additional peaks corresponding to hexagonal $P6_3/mmc$ indicative of bulk ruthenium metal, indicating that the metal is well-dispersed with small crystallite size. Additionally, the lattice parameters of the supports do not vary significantly following ruthenium-loading.

Ruthenium nanoparticles can be seen on TEM micrographs which confirms successful catalyst formation by wet-impregnation and reduction of Ru(acac)$_3$ (Figure 2). Nanoparticle size for each catalyst was averaged over 50 measurements from several images. All distributions show a mean particle size of less than 7 nm. The non-, Ho- and Y-doped supports exhibited lower particle size, <5 nm; meanwhile Er- and Yb-doped supports exhibited larger particles, 5.9 nm and 6.9 nm, respectively.

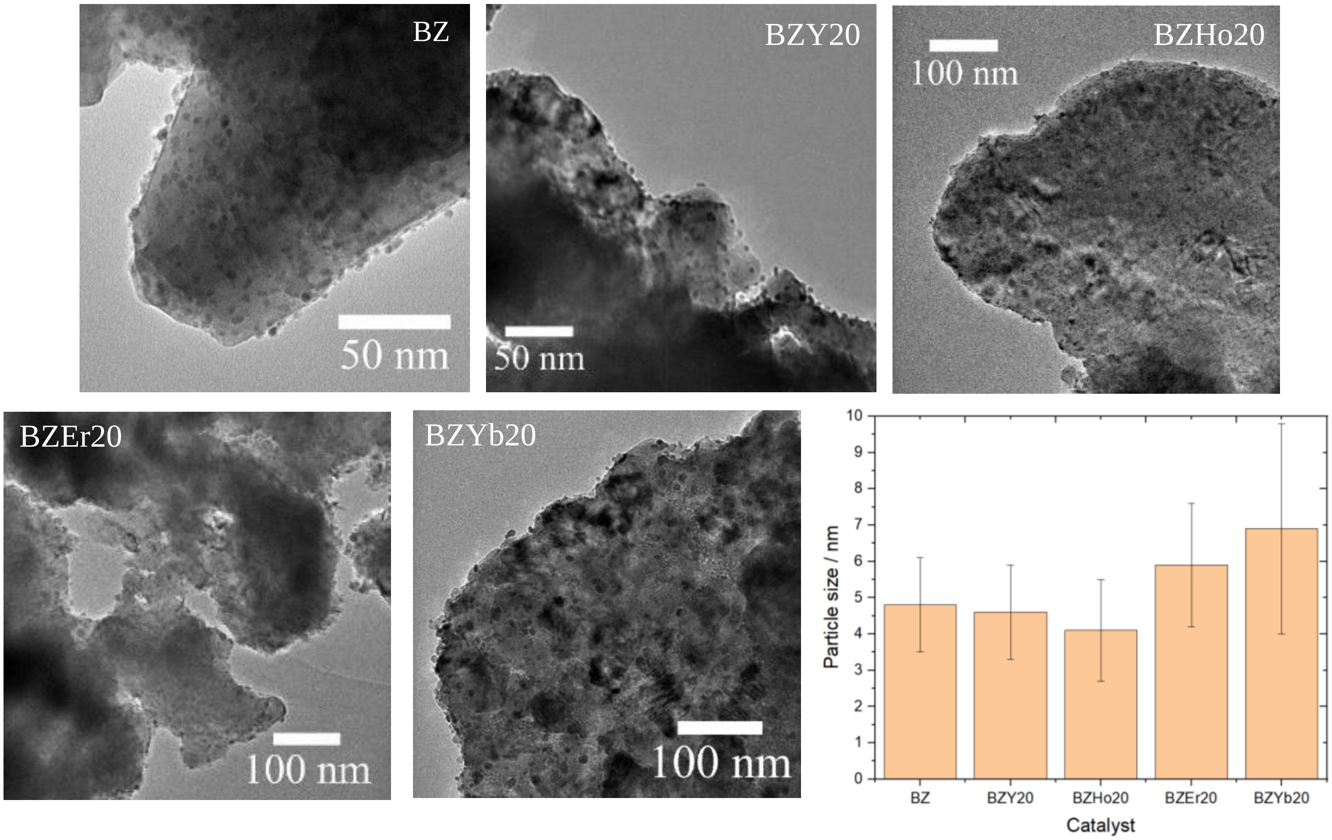

Figure 2. TEM micrographs of several ruthenium catalysts supported on rare-earth-doped BZ, and mean ruthenium particle size from 50 measurements across multiple micrographs for each sample. Histograms shown in Figure S4.

The range of rare-earth-doped BZ catalysts derived from $Ru(acac)_3$ were synthesised and tested on a fixed-bed reactor for ammonia synthesis: $BaZr_{0.8}M_{0.2}O_{3-\delta}$, M = Y, Ho, Er, Yb. It was observed that a change of support had a dramatic effect on the initial rate of ammonia synthesis (Figure 3). However, the catalysts suffer from progressive deactivation. The highest initial rate was yielded by the yttrium-doped support RuBZY20, and the lowest rate by the non-doped RuBZ catalyst. The other rare-earth-doped catalysts all showed modest rates: Y > Ho > Yb > Er > non-doped BZ according to our catalytic testing. This indicates the nature of aliovalent element can play an important role on the ammonia synthesis rate. However, at first glance, these rare-earth-doped BZ samples do not show any direct correlation with bulk proton conductivity or proton transport activation energy (Ho > Y > Er > Yb)[54], proton-induced lattice strain (Yb > Y > Ho > Er)[54], or ruthenium nanoparticle size (Figure S5). But, the series seems to correlate better with the previously measured proton concentration (Y > Ho > Er > Yb) by Han et al.[54]. It is postulated that the size of the proton reservoir offered by the perovskite support significantly affects the rate of ammonia synthesis. Nevertheless, correlating this behaviour to this single property does not give a perfect match, and instead the kinetics of the reaction may relate to a convolution of these and other factors.

Varying yttrium-doping

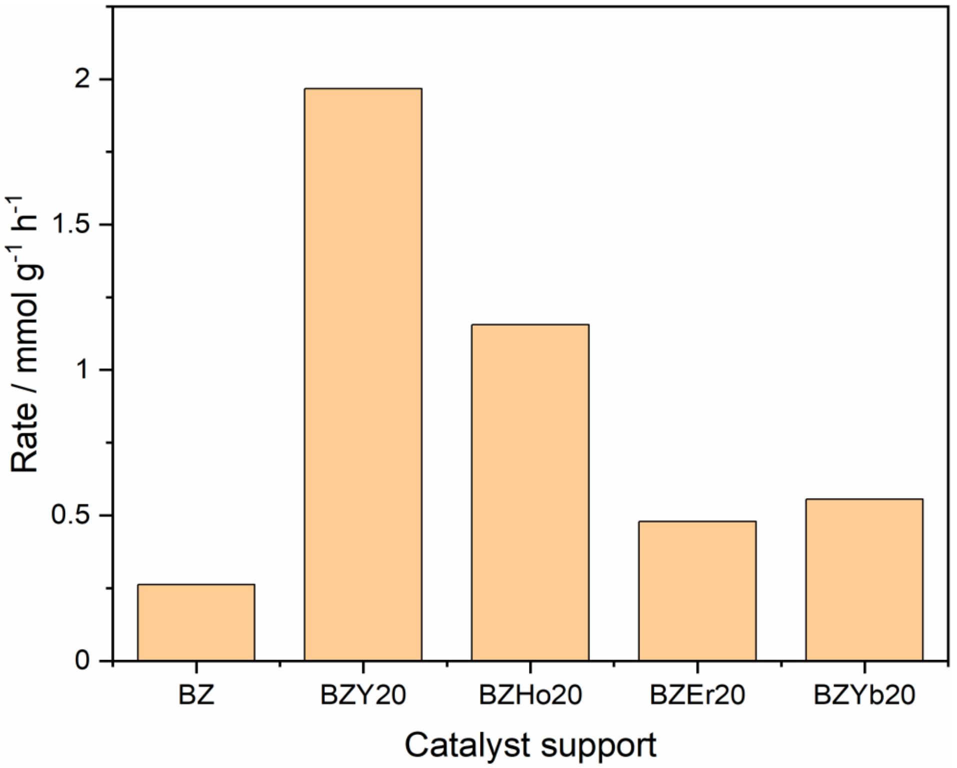

Figure 3. Initial rates of ammonia synthesis for BZ supports doped with various rare-earth metals.

Having found that yttrium is the most effective dopant for ammonia production, the degree of doping was investigated. A series of yttrium doped barium zirconate supports was synthesised: $BaZr_{1-x}Y_xO_{3-\delta}$, where $x = 0, 0.1, 0.2,$ and 0.5, i.e. undoped BZ, BZY10, BZY20, BZY30 and BZY50, which were confirmed by synchrotron X-ray powder diffraction (SXPD) (

Figure 4). Increasing the degree of doping of yttrium, which is a larger ion than zirconium, is shown to linearly increase the lattice parameter. It has been reported for the BCY system that the level of B-site doping can induce ordered octahedral distortion, hence reducing the symmetry, and altering the space group of the crystal[55]. This can usually be observed by the resolution of shoulder peaks as the equivalence of symmetry-related reflections is broken, i.e. reducing the multiplicity of peaks, resulting in more peaks. However, on interrogation of our SXPD data, we see no evidence of any change in symmetry. Some disordered octahedral tilting is known for the BZY system through IR characterization[56]. They have ascribed the decreasing proton conductivity above 20%Y, despite increasing proton concentration, to local distortions which form less favourable proton traps. The observations reported in this work agree with this hypothesis.

Elemental analysis showed that the target yttrium occupancy of the B-site was achieved to high accuracy (Ru-BZY20: 19.39% Y) (Table S2). It is interesting to reveal from the Figure 4 that there is a clear volcano-dependence of initial activity with respect to Y-doping. The optimal initial activity value corresponds to 20%Y. It is accepted that the introduction of Y in B site can enhance the oxygen vacancy concentration. The yttrium incorporation takes place continuously up to 50% as observed in the linearly increasing lattice parameter. However, the increasing oxygen vacancy concentration does not seem to monotonically facilitate the promotion of ammonia synthesis by proton hopping over dynamic surface hydroxyl beyond *x* = 20 (Scheme 1), with higher yttrium doping being detrimental to the reaction rate.

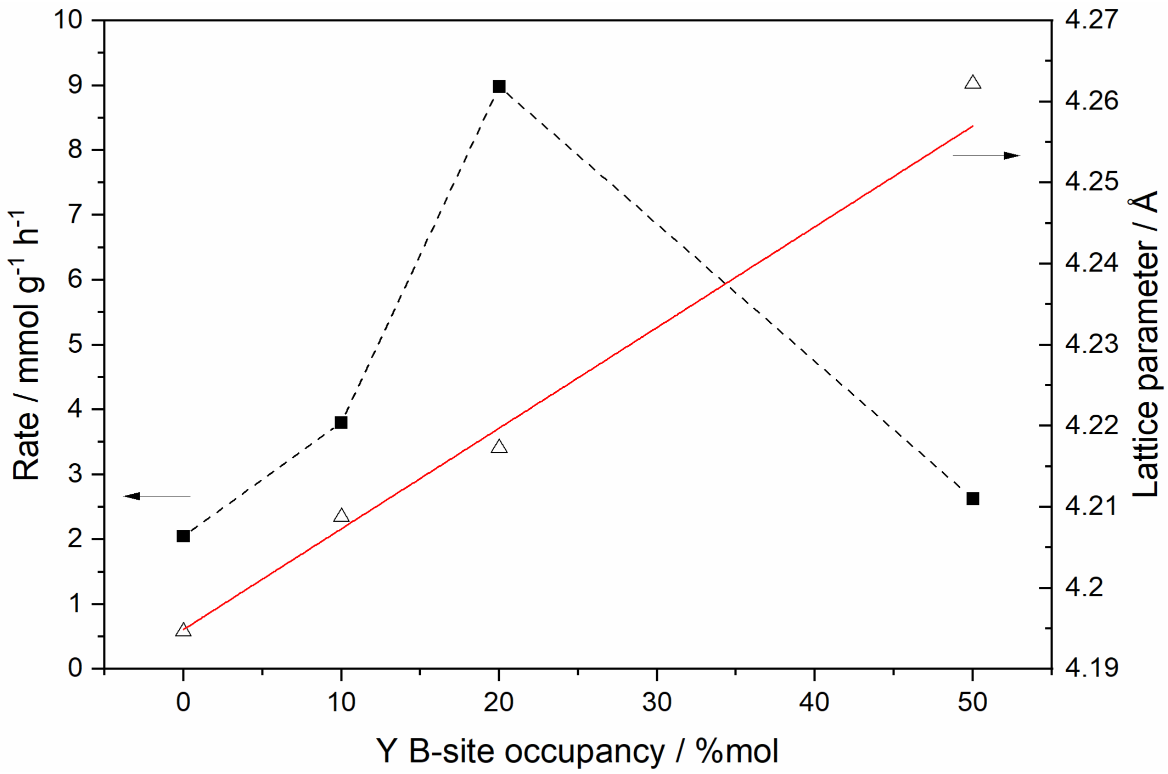

Figure 4. Initial rates of ammonia synthesis over the supported ruthenium catalysts per total mass of catalyst; lattice parameters (SXPD) of non-ruthenium supported BZ perovskites with increasing yttrium-doping; p_{H2}:p_{N2} = 3:1, 50 bar total pressure, 50 mL min^{-1} flow, 450°C.

Notice that Shimoda et al.[57] also found a volcano-type correlation, which they reported to peak at BZY10; however they did not elaborate on the trend. We attempted to link this catalytic behaviour with the protonic conductivity values reported by Han et al.[40] and others[56] over these doped perovskites. Indeed, they showed the greatest bulk, grain-boundary and total conductivity at 10mol% to 20mol% doping, followed by a similar decrease for 25%mol and above. It is also known that increasing yttrium-doping leads to decrease proton transport activation energies[58]. As stated, it is clear that the rate of ammonia synthesis is highly dependent on proton transport in avoiding hydrogen poisoning for nitrogen activation. Here, we present evidence for a hydrogen spill-over mechanism facilitated by the BZY support, which results in the alleviation of hydrogen poisoning on the ruthenium surface and the electronic promotion of dinitrogen dissociation. Further increase in Y-doping appears to offer stronger proton trap sites to account for the decrease in proton conductivity.

Kinetic investigations

In order to ascertain the alleviation of hydrogen poisoning and having found that BZY20 is the most effective support at 450°C, an in-depth kinetic investigation was carried out on the yttrium doping of caesium-promoted 15%wt ruthenium catalysts. Catalysts were doped with caesium, which is a well-known electronic and structural promoter. Electronic promotion operates by increasing the back-bonding from the ruthenium metal into the dinitrogen anti-bonding orbital, which facilitates bond breaking and reduces the kinetic barrier. Structural promotion is the prevention of ruthenium sintering and catalyst deactivation. Hence, caesium was used in order to achieve maximal rates with good catalyst stability for reliable kinetic studies and comparison to literature-best values. The catalysts Cs-RuBZ, Cs-RuBZY10, Cs-RuBZY20, and Cs-RuBZY30 were synthesised and tested over a range of p_{H2}, from 1.25 bar to 7.5 bar, and at 425°C and 450°C. The effect of the caesium can clearly be seen in the increased rates, which are an order of magnitude greater than those without caesium, and enhanced stability over 24 hours on-stream (Figure S6).

As was the case above, low levels of yttrium-doping improved the catalytic performance significantly and then followed a volcano-type dependence (Figure 5). As discussed, this is in agreement with the reported values for intra-grain conductivity. Interestingly, the rates of reaction for BZ, BZY10, and BZY20 were lower at 450°C than 425°C (Figure 5). The peak rate at 450°C (BZY20, 47 mmol h^{-1} g^{-1}) was lower than the peak rate at 425°C (BZY10, 65 mmol h^{-1} g^{-1}), which is the highest rate for any catalyst reported in this work. This volcano-type dependence on temperature is due to the increasing significance of the backward reaction to hydrogen and nitrogen at higher temperatures, which considerably reduces the observed rate of ammonia synthesis. The conversion at 425°C is recorded as 2.37%, and decreases at 450°C to 2.21% (Figure S7). This decrease is observed for BZ, BZY10, and BZY20. This decreasing activity at 450°C nearing the equilibrium is also shown for this system by Shimoda et al.[57]. However, the conversion and rate of reaction for BZY30 increases at 450°C. It is postulated that such high yttrium doping at 425°C offers an additional effect of stronger kinetic hydrogen trapping which restricts the kinetics relative to 450°C. Indeed, BZY20 does not exhibit as large a decrease in conversion and rate than BZY10.

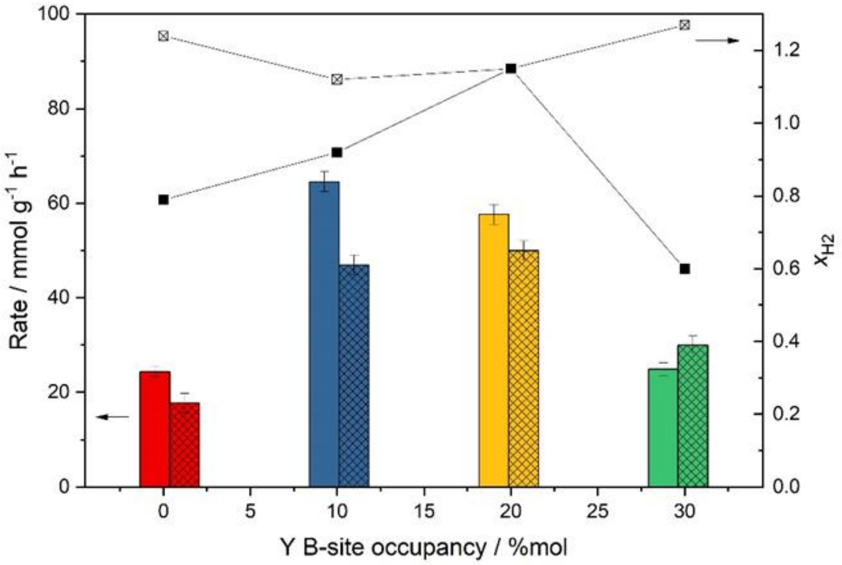

Figure 5. Rates (columns) and H_2-orders (scatter, derived from Figure S8) of Cs-RuBZY catalysts against yttrium-doping at 425°C (filled) and 450°C (crossed); p_{H2} = 7.5 bar, p_{N2} = 2.5 bar, GHSV = 12400 h^{-1}.

This rate performance is exemplary compared to many supported ruthenium catalysts (only measured rates with equivalent conversions below 20% of the equilibrium value were used for comparison) (Table S1). At 400ºC, the Cs-Ru/BZY20 catalyst performs better than most catalysts reported in literature, with the exception of the reports by Kitano et al.[59] and Ogura et al.[60] Critically, it outperforms the barium zirconate-based catalysts of Wang et al.[27] and Shimoda et al.[61] Though other supports such as $La_{0.5}Ce_{0.5}O_{1.75}$ and MgO(111) give more active catalysts when considered on a per mole ruthenium basis.[60,62]

The extent of hydrogen poisoning was investigated by probing the order of reaction with respect to hydrogen (x_{H2}). This type of kinetic measurement will only be valid if the reaction takes place far from the equilibrium, ensured by using high flowrates. Up to and including temperatures of 425°C, for which the conversions are far from equilibrium, the increases in rate with yttrium-doping is attributed to the increased ability of the support to alleviate hydrogen poisoning. This results in increased hydrogen partial pressure to accelerating the reaction as a reactant rather than hindering it through preferential adsorption at active ruthenium sites. In the HB process, hydrogen poisoning is observed by negative values of x_{H2} (~-1)[6,21,28,30]. Here, however, it is noted that all x_{H2} values are still appreciatively positive, often exceeding 1, which shows that dihydrogen is significantly contributing to the rate of reaction as a reactant rather than as a poison over this type of catalyst under this reaction temperature (Figure 5 and Figure 6b). In fact, we show that much higher rates were observed for the catalysts that exhibited highly positive x_{H2} (moderately-doped supports BZY10 and BZY20) due to more mobile surface hydrogen and site availability, whilst low rates were observed for catalysts that exhibited lower x_{H2} order (non-doped BZ and highly-doped BZY30) due to lower surface hydrogen dynamics (Figure 6b).

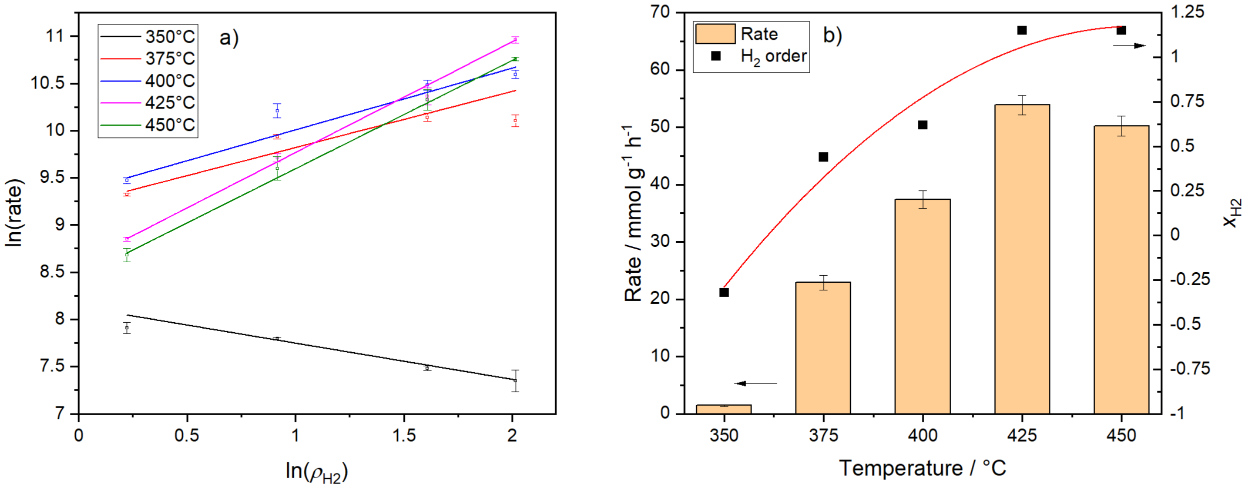

Figure 6. Kinetic study of Cs-RuBZY20. (a) Rates of reaction at various hydrogen partial pressures; (b) peak rate of ammonia synthesis (ρ_{H2} = 7.5 bar) and hydrogen order at each temperature.

It is further shown that preventing hydrogen poisoning is more crucial for efficient ammonia synthesis rate by conducting the catalysis at lower temperatures. The catalyst BZY20 was then tested at the 400°C, 375°C, and 350°C (Figure 6), for which the rate and x_{H2} values indeed gradually decreased. Reducing the temperature from 375°C to 350°C reduced the rate of reaction by an order of magnitude, which can be explained by an appreciably negative x_{H2}. This is consistent with the principle that hydrogen poisoning is more significant at lower temperature due to hydrogen preferential adsorption than nitrogen at B5 sites[63]. Under the same low temperature conditions, almost no activity was recorded over the non-doped BZ and highly-doped BZY30.

As a result, it is shown that 425°C is the optimal temperature for these catalysts and conditions. The moderately-doped supports BZY10 and BZY20 exhibited the highest rates of ammonia synthesis through effective hydrogen-poisoning alleviation to keep surface hydrogen mobility, which is shown to be a very important aspect of the reaction kinetics. This alleviation is shown to be highly dependent on yttrium-doping, which affects several physical properties such as oxygen vacancy concentration, and both protonic and electronic conductivity. Comparatively, at 425°C, BZY20, which exhibits the highest x_{H2} order and the highest rate reported in this work, is also known to be the optimum yttrium-doping with for electronic and protonic conductivity. In addition, a significant deviation of the apparent activation energy from typical ~100 kJ mol^{-1} [63,64] to 27-42 kJ mol^{-1} at lower temperature regime over the moderate doped samples was recorded (Figure S9). A hydrogen spill-over mechanism that is facilitated by aliovalent doping and good conduction properties is proposed in order to explain the effective alleviation of poisoning of these materials.[55]

In-situ X-ray Photoelectron Spectroscopy

In order to further observe the spill-over of hydrogen from ruthenium to support, near-ambient pressure in-situ XPS (NAP-XPS) was used to characterise ruthenium and oxygen environments when exposed to hydrogen and argon atmosphere alternatively at 450°C (B07 beamline, DLS). By analysing in-situ changes in the O 1s and Ru 3d binding energies, we have observed, respectively, the effect of hydrogenation on the chemical environment of perovskite lattice oxygen, and the degree of electron transfer to ruthenium, i.e. electronic promotion which increases catalytic activity. In order to remove the electronic promoting effect of the caesium dopant, non-doped perovskite-supported ruthenium catalysts were characterised: RuBZ, RuBZY10, RuBZY20, and RuBZY30. Full spectra and tabulation shown in Figure S10.

The catalysts under initial hydrogen atmosphere show significant differences as a result of yttrium-doping. To first interrogate the oxygen environment (oxide: 531 eV, hydroxyl: 532 eV), interestingly, the moderately-doped supports (BZY10 and BZY20) contain predominantly hydroxyl species (-OH: 75-90%) showing the highest percentage of hydroxyl over all conditions, and also the strongest atmosphere-dependent change in their surface oxygen to hydroxyl composition. Meanwhile the non-doped and highly-doped supports (BZ and BZY30) are predominantly composed of oxide species (-OH: 47-49%) (Figure 7). Hence it is shown that there is not a linear correlation between yttrium-doping and spill-over of hydrogen adatoms. This is in agreement with the catalytic data reported herein, in which the activity BZY30 was much lower than BZY10 or BZY20. The additional hydroxyl composition of ~25% is attributed to the presence of aliovalent yttrium for both BZY10 and BZY20 that can accept higher proton incorporation through charge-balancing arguments. However, it is noted that the hydroxyl composition is much higher than might be predicted by the degree of aliovalent yttrium-doping and the associated charge balancing arguments. Assuming the formation of two oxygen vacancies for each yttrium atom, and their electronic quenching by water to form two lattice hydroxyl species (Equation 2), an upper limit of 3.3% of oxygen atoms are expected to be observed as hydroxyls (this estimate can be doubled to 6.7% by assuming hydrogen bonding[37]). But such a value is still far below the OH/O values we observed by NAP-XPS. Thus, it cannot be accounted by the stoichiometry due to Y^{3+} substitution to Zr^{4+} to form Y-O(H)-Zr but attributed to the proton migration from the pre-reduction of Ru^{2+} ($Ru^{2+} + H_2 = Ru + 2H^+$) and spill-over hydrogen from ruthenium catalyst nanoparticles to other surface sites of the oxide support especially over the moderately-doped supports (BZY10 and BZY20). Notice that the NAP-XPS is mainly measuring the surface composition (different from the bulk values).

When the catalysts are exposed to argon, the composition of oxide increases particularly in the moderately doped supports, which shows some degree of hydroxyl conversion to oxide is reversible. However, the moderately-doped supports still exhibit high hydroxyl composition due to kinetic stable OH over the surface trapped sites. This indicates that even when reversible hydrogen spill-over is not operative, many more protons can be accommodated in these structures than BZY or BZY30. Changing the gas back to hydrogen causes the hydroxyl levels to recover in the moderately-doped supports and highly-doped BZY30. The non-doped BZY exhibits little change, in fact exhibiting slightly more oxide species.

A similar change is also seen in the ruthenium binding energy (Figure S10), which is directly affected by the spill-over by electronic promotion. However, only BZ and BZY20 with resolved ruthenium signals were able to be analysed due to poor intensity. Upon exposure to hydrogen, argon and hydrogen alternatively, the non-doped BZ gave similar Ru $3d_{5/2}$ binding energy (280.43 ± 0.05 eV) which corresponded to ruthenium metal nanoparticle value. However, the RuBZY20 catalyst exhibited the behaviour predicted by the proposed hydrogen spill-over mechanism. The low Ru $3d_{5/2}$ binding energy under hydrogen (280.18 ± 0.05 eV) is indicative of the slight increased occupancy of the Ru 3d band due to donation from the support, which can aid dinitrogen reduction. Under argon, the binding energy increases

(280.73 ± 0.05 eV). On the re-introduction of hydrogen, the binding energy returns to the same value, indicating the reversibility of the electron transfer, and reinforcing the observation in the O 1s region.

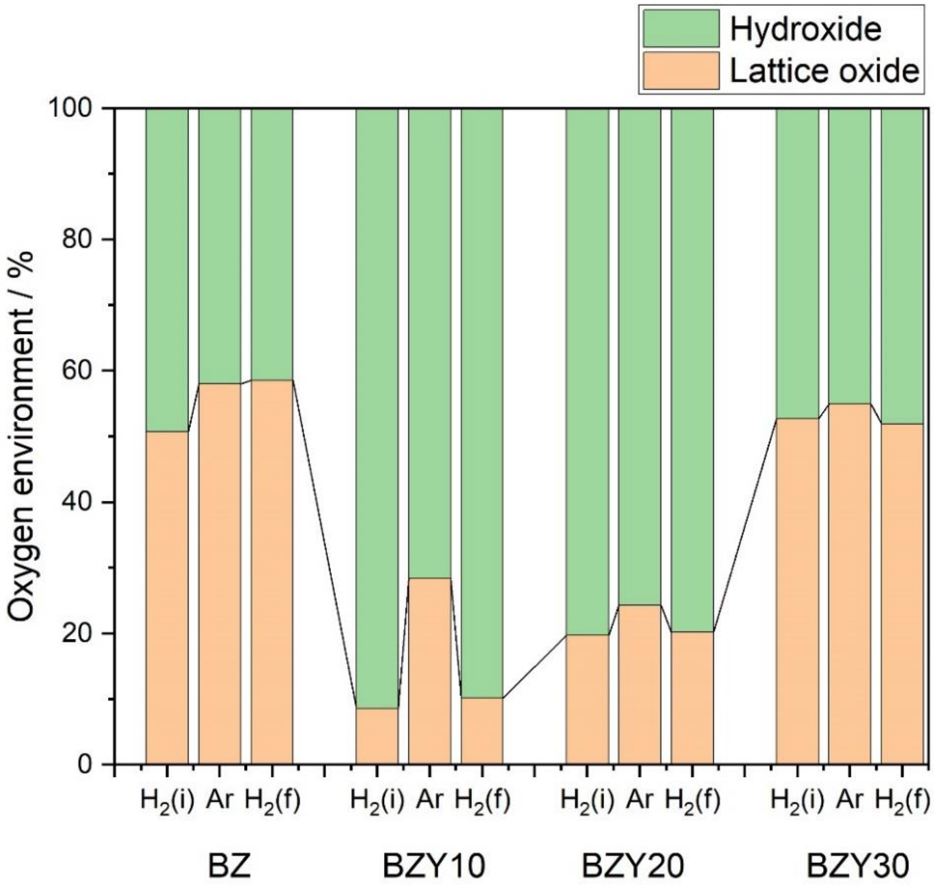

Figure 7. In-situ NAP-XPS of RuBZ, RuBZY10, RuBZY20, and RuBZY30 (left to right) under initial hydrogen (H_{2i}), argon (Ar), then hydrogen (H_{2f}). (a) Oxygen composition of oxide (531 eV) (blue) and hydroxyl (532 eV) (orange). (b) Binding energy of Ru $3d_{5/2}$.

Neutron Powder Diffraction

Having identified the lattice hydroxyl species through electronic effects of the support and ruthenium, direct observation was sought by crystallography. X-ray diffraction methods are not capable of resolving hydrogen due to its low electron density which furthermore has strong anisotropic association with nearby atoms. Meanwhile, deuterium is easily resolved in neutron diffraction experiments due to its high neutron scattering length, even amongst electron-rich elements such as barium and ruthenium.[57,58]

As for NAP-XPS, non-caesium-doped catalysts were characterised: pristine BZY20 and 15%wt RuBZY20. The ability of BZY20 to accommodate hydrogen was tested by exposing both the pristine support and 15%wt ruthenium catalyst to D_2O under saturated argon flow at 600°C; non-deuterium doped samples were also heated to 600°C but under dry argon flow. Diffraction data was collected at room temperature (Figure 8). A Pawley refinement was carried out on the BZY20 using a single phase of the known perovskite space group $Pm\overline{3}m$, yielding a lattice parameter of (a_{sup} = 4.2259 Å) and acceptable residuals (R_{wp} = 3.74%; *GoF* = 6.17). The pattern for RuBZY20 yielded a slightly smaller lattice parameter for the support (a_{sup} = 4.222 Å), and also a metallic ruthenium phase ($P6_3/mmc$, a_{Ru} = 2.70 Å, c_{Ru} = 4.28 Å) (R_{wp} = 2.88%; *GoF* = 3.73) (Table 1).

Table 1. Pawley refinement of neutron diffraction data of BZY20 and RuBZY20.

	Material	BZY20	RuBZY20
Residuals	R_{wp} / %	3.74	2.88
	GoF	6.17	3.73
BZY20	a_{sup} / Å	4.22590(8)	4.2218(8)
Ru	a_{Ru} / Å	N/A	2.6971(9)
	c_{Ru} / Å	N/A	4.283(1)

Rietveld refinement was used to elucidate the ABO_3 perovskite structure (full refinement details shown in Table S3). The refinement was prepared with the following values, then freely allowed to refine: lattice parameters from Pawley refinement, perovskite site occupancy as predicted by the reaction stoichiometry ($BaZr_{0.8}Y_{0.2}O_{3-\delta}$), thermal parameters at unity. All atomic positions were fixed at their known values, and occupancy and thermal parameter for the ruthenium site fixed at unity. A reasonable structure was found for both pristine and ruthenium-dispersed samples, for which the fitting parameters were sufficiently low, $R_{\mathrm{wp}} < 4\%$.

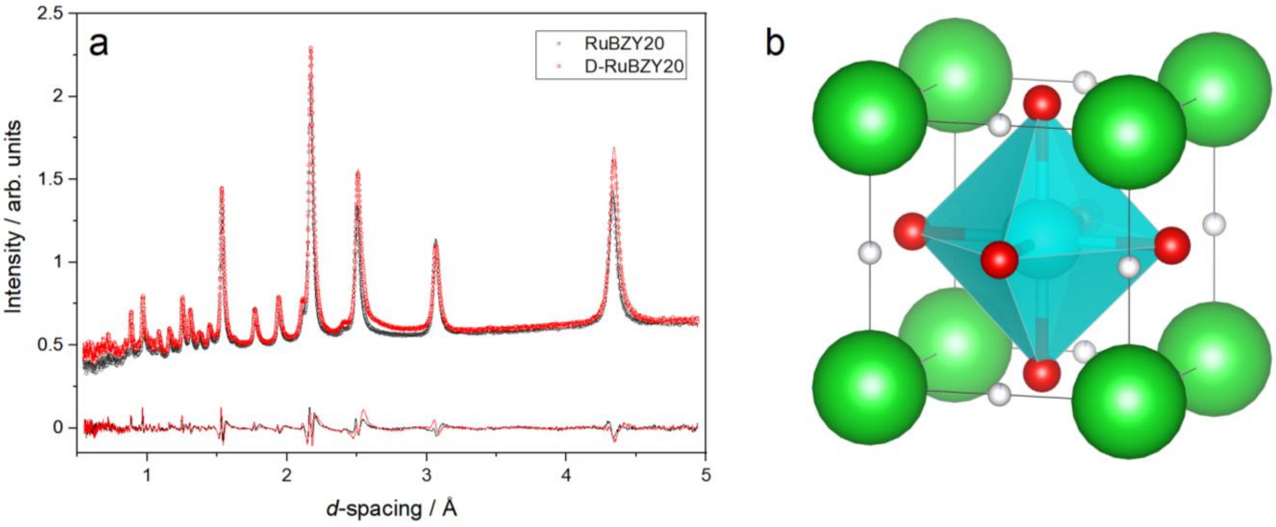

Figure 8. (a) Observed neutron diffraction patterns and Rietveld fit for RuBZY20 and D-RuBZY20. (b) Unit cell of structure solution for D-RuBZY20.

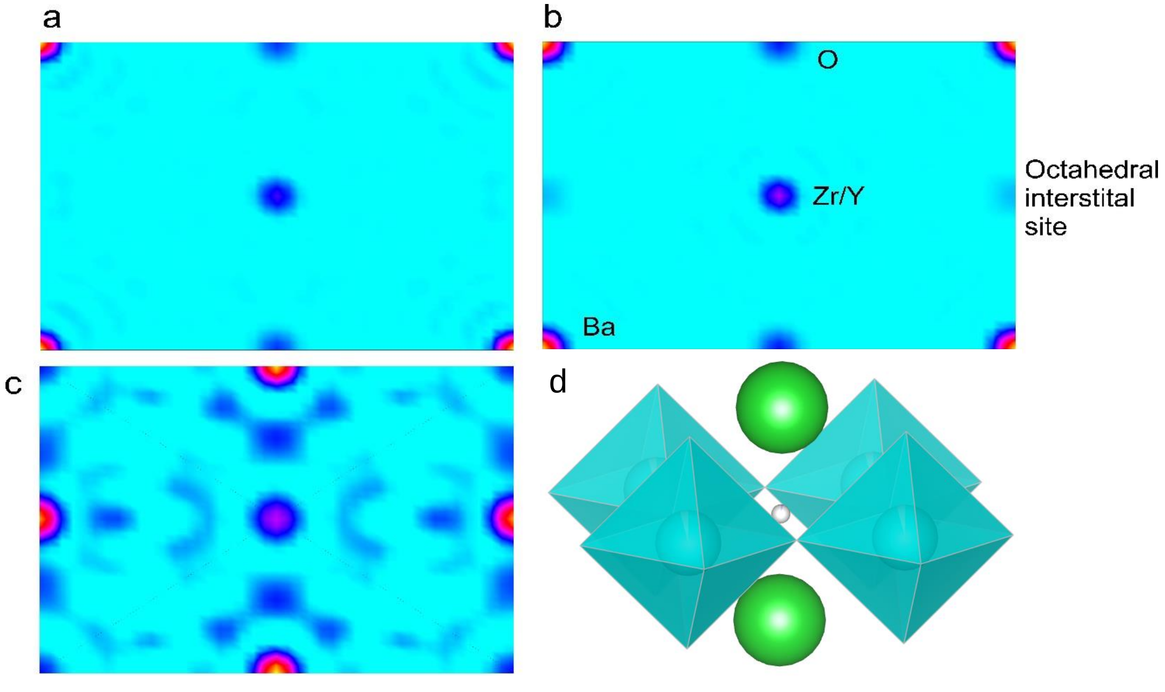

Figure 9. Fourier synthesis of observed neutron-scattering-length density using observed structure-factor amplitudes and phase information from Rietveld structure solution of BZY20 support at 1×*d* [Å] along the (011) plane; only positive density of neutron scattering length shown; maximum saturation at maximum scattering length density, minimum saturation at zero scattering length density: (a) non-deuterated, (b) deuterated. (c) Fourier difference map ($F_{obs} - F_{calc}$) of the deuterated support D-BZY20 (saturation / [10^{12} cm $Å^{-3}$]: min = 0; max = 0.045). (d) Local environment of the interstitial deuterium site.

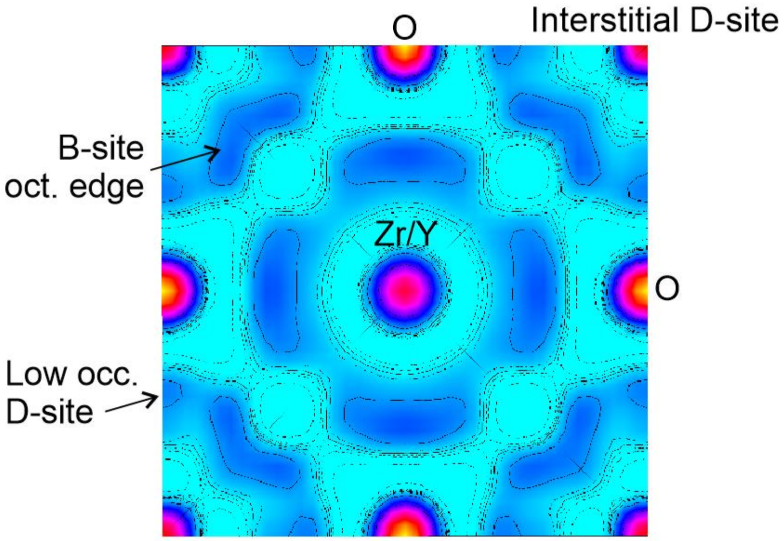

Figure 10. Fourier synthesis of neutron-scattering-length density difference ($F_{obs} - F_{calc}$) from Rietveld structure solution of D-RuBZY20 support at 0.5×d [Å] along the (001) plane, showing diffuse neutron-scattering-length density within the B-site octahedron (between O^{2-} and B-site), and along the B-site octahedral edge (between O^{2-} sites).

The diffraction patterns for deuterated samples exhibited greater intensity peaks, which is attributed to additional neutron-scattering-length density due to the presence of interstitial deuterons in the perovskite lattice. Expectedly, the phases retrieved from the Rietveld structure solution were the same for the deuterated and non-deuterated patterns. When these phases were applied to the observed structure factors, a reverse Fourier transform yields neutron-scattering-length density maps (Figure 9). The Fourier synthesis of the deuterated sample clearly shows scattering-length density mainly at an interstitial site formed by between two trans A-sites and four mutually-cis B-sites Zr/Y tetrahedra. These surrounding atoms form an octahedron of sorts; hence the site is referred to as the interstitial octahedral site. This interstitial site has also been shown to be able to accommodate nickel atoms by Han et al.[65] This site can be seen more clearly in the Fourier difference map of D-BZY20 (Figure 9). Here, the missing atom at the octahedral site is very prominent. The A- and B-sites are modelled reasonably well, though there is also additional neutron-scattering-length density at the oxygen site which is unaccounted for. This interstitial deuterium site is also seen in the deuterated sample with supported ruthenium, D-RuBZY20. The presence of deuterons within the support lattice is consistent with the known proton conductivity of these perovskite materials. The intercalation is further observed through an expansion of the unit cell by ~0.008 Å following deuteration for both the pristine and ruthenium patterns. The refined phase compositions of ruthenium for both RuBZY20 and D-RuBZY20 are ~1.4%wt. This is deviated from the ICP-MS result, which is deemed to be more accurate. The discrepancy is attributed to an appreciable population of ruthenium nanoparticles below 5 nm, which do not contribute to observable Bragg scattering; this is similar to the absence of a ruthenium phase in patterns collected using laboratory-source X-rays discussed above.

The presence of ruthenium increases the deuterium occupancy from 3.74% to 4.79%. Expressed as a relative change, this equates to a 28% increase in the incorporation of deuterium. The deuterons present in the non-ruthenium support are attributed to water splitting by the support itself (Equation 2). The presence of ruthenium evidently increased the supply of deuterium and shifted the equilibrium towards lattice hydroxyls. Notice that the mulitplicity of the interstitial site (Wyckoff: 3d) produces three-times the site occupancy value across the unit cell, resulting in a D/Y ratio of 0.7 for the support with ruthenium .

The location of the deuterium site is unexpected. In other aliovalent-doped perovskite systems, protons have been observed closely associated with a single oxygen site (~1.0-1.2 Å)[37,66,67] located on the face of the unit cell. Here, the deuterium is at a high symmetry site, which is equidistant from four oxygen atoms in a plane and two barium atoms that lie above and below the plane, forming an octahedral coordination, though any formal bonding seems speculative. As a consequence, the deuterium is not singularly associated with one oxygen and is much further away from any oxygen (2.1 Å). This distance is more similar to the length of hydrogen bonding found in other perovskite systems.[67,68] There, they admit that the asymmetric location that results from hydrogen bonding has unknown effects on proton mobility; this is namely in that the proton is indeed more proximal to the next oxygen, but is trapped in moderately formal bonding. We postulate that the far greater than expected hydroxide composition as shown by NAP-XPS, could be due to this extended association of deuterium with four oxygen atoms.

It has previously been shown that protons may transitionally pass near to the interstitial octahedral site as part of the bulk migration mechanism (Scheme 1). For Zr-O(H)-Zr moieties, the energy barrier to intra-octahedral (re-orientational/local) and inter-octahedral (jump/bulk conduction) migration are equivalent.[37] However, it is also reported that a low energy, strong proton trap is centred around YO_6 octahedra for which the proton is involved in local charge-balancing; while the barrier to intra-octahedral mobility is unchanged, an additional energy barrier must be overcome in order to continue to contribute to bulk proton conduction.[37] We ascribe the significant symmetric nuclear density at the octahedral site to be the direct visualization by NPD of a weakly trapped deuterium structure. The observation of a deuterium site that is weakly associated to oxygen is reasonable since these sites are larger in quantity than the strong proton trap sites Y-O(H)-Zr at the interface given that the yttrium-doping is not high. It is also noted that this crystallographic analysis yields an average structure over both time and the sample ensemble. However, it is deemed unlikely that such strong atomistic (that is to say, spherical) nuclear density is a result of either spatially averaged traps or significantly increased proton dynamics.

Nuclear density is observed at a more conventional site that is strongly associated with one oxygen atom at a distance of 0.93 Å. This agrees with the existence of a weak proton trap sites alongside stronger deep trap sites, which has been previously shown by both molecular quantum dynamics simulations and quasi-elastic neutron scattering studies[32]. However, this strong site is difficult to model due to the weak signal/occupancy and surrounding volumes of diffuse and similar nuclear density. This is non-negligible scattering-length density along the edges of the B-site octahedra between oxygen sites (Figure 10), which is similar to a previous siting of a proton trap in aliovalent-doped octahedra by Ito et al.[69], particularly at low temperatures. Hence, the diffuse scattering density here is attributed to some of these trapped deuterium ions with increased thermal mobility. It is concluded that the lack of observed atomicity prevents the reasonable modelling of a discrete crystallographic site for either the slightly atomistic strong trap or diffuse octahedral edge. Hence, we have observed deuterium for the first time at a weak mobile trap at the octahedral hole at higher quantity, and along with the stronger trap near oxygen sites of octahedra and perhaps associated with interfacial oxygen with aliovalent yttrium at lower quantity. Notice that by using NMR on Grey et al. have also observed proton spots in proton conductive related doped perovskites at low temperature, which may also correspond to the proton trapped sites over these structures[68].

Conclusions

Ruthenium nanoparticles have been supported on a range of rare-earth-doped barium zirconate perovskite supports. We show that yttrium-doped supports are by far the most active promoter of ammonia synthesis. Initial catalytic testing under high pressure and moderate flow rates showed BZY10 to be most effective level of doping at 425°C, and BZY20 at 450°C, increasing from the non-doped support by an order of magnitude, which was linked to the support's high proton conductivity. Structural and electronic promotion was achieved by doping the ruthenium catalyst surface with caesium, improving the rate of reaction by an order of magnitude and eliminating catalyst deactivation by reducing sintering.

The kinetics of the more stable caesium-promoted catalysts were investigated under high flow rates and moderate pressure. Optimal conditions and doping-level was again found to be 10%mol to 20%mol Y dependent on reaction temperature. The study of hydrogen-order dependence on dihydrogen showed the effective alleviation of hydrogen poisoning by the hydrogen spill-over effect over these BZY samples. The atmosphere-dependent change of oxygen environment in the support from oxide to hydroxyl was observed by in-situ NAP-XPS. It is thus concluded that for high rates of ammonia synthesis, the BZY support facilitates N_2 activation on Ru metal surface without the competition of strong hydrogen adsorption. As a result, the proton conductivity of the support is crucially important, which is characterized by a proper balance of oxygen vacancy concentration (B-site doping), trapping-site concentration and their proton hopping activation energy (lattice parameter dependent). The presence of hydrogen species in both weakly and strongly bound states within the lattice was first identified by neutron powder diffraction in this work.

Supporting Information

Additional experimental results including TEM micrographs, ICP-MS, XRD patterns and parameters, long-duration catalytic tests and plots of kinetic investigations, discussion on conversion and equilibrium, comparisons of catalytic activities to other works, detailed tabulation and plots of NAP-XPS, and detailed parameterization of NPD refinement.

Acknowledgements

The support for this project from the EPSRC in the United Kingdom (1947428) is gratefully acknowledged. CF and JF give thanks to EPSRC for a joint DPhil Studentship with Diamond Light Source and Siemens, respectively. The authors also acknowledge the use of NAP-XPS facilities and XRD facilities at beamlines B07 and I11 at Diamond Light Source, UK.

Notes

The authors declare no competing financial interest.

References

(1) Haber, F.; Le Rossignol, R. Über Die Technische Darstellung von Ammoniak Aus Den Elementen. *Z. Für Elektrochem. Angew. Phys. Chem.* **1913**, *19* (2), 53–72. https://doi.org/10.1002/bbpc.19130190201.

(2) Apodaca, L. *Nitrogen Statistics and Information: NITROGEN (FIXED)—AMMONIA*; Nitrogen Statistics and Information; United States Geological Survey, 2020; pp 116–117.

(3) Smil, V. Detonator of the Population Explosion. *Nature* **1999**, *400* (6743), 415–415. https://doi.org/10.1038/22672.

(4) Zamfirescu, C.; Dincer, I. Using Ammonia as a Sustainable Fuel. *J. Power Sources* **2008**, *185* (1), 459–465. https://doi.org/10.1016/j.jpowsour.2008.02.097.

(5) Review and Evaluation of Hydrogen Production Methods for Better Sustainability. *Int. J. Hydrog. Energy* **2015**, *40* (34), 11094–11111. https://doi.org/10.1016/j.ijhydene.2014.12.035.

(6) Siporin, S. E.; Davis, R. J. Use of Kinetic Models to Explore the Role of Base Promoters on Ru/MgO Ammonia Synthesis Catalysts. *J. Catal.* **2004**, *225* (2), 359–368. https://doi.org/10.1016/j.jcat.2004.03.046.

(7) Darwent, B. deB. *Bond Dissociation Energies in Simple Molecules*; NSRDS-NBS31; U.S. National Bureau of Standards; for sale by the Supt. of Docs., U.S. Govt. Print. Off.: Washington, 1970.

(8) Emmett, P. H.; Brunauer, S. The Adsorption of Nitrogen by Iron Synthetic Ammonia Catalysts. *J. Am. Chem. Soc.* **1934**, *56* (1), 35–41. https://doi.org/10.1021/ja01316a011.

(9) Mittash, A.; Frankenburg, W. *Adv Catal* **1950**, *2*, 81–104.

(10) Erisman, J. W.; Sutton, M. A.; Galloway, J.; Klimont, Z.; Winiwarter, W. How a Century of Ammonia Synthesis Changed the World. *Nat. Geosci.* **2008**, *1*, 636.

(11) Ertl, G. Surface Science and Catalysis—Studies on the Mechanism of Ammonia Synthesis: The P. H. Emmett Award Address. *Catal. Rev.* **1980**, *21* (2), 201–223. https://doi.org/10.1080/03602458008067533.

(12) Nature of Nitrogen Adsorbed on Transition Metal Surfaces as Revealed by Electron Spectroscopy and Cognate Techniques. *Surf. Sci. Rep.* **1991**, *13* (7), 223–263. https://doi.org/10.1016/0167-5729(91)90014-O.

(13) Foster, S. L.; Bakovic, S. I. P.; Duda, R. D.; Maheshwari, S.; Milton, R. D.; Minteer, S. D.; Janik, M. J.; Renner, J. N.; Greenlee, L. F. Catalysts for Nitrogen Reduction to Ammonia. *Nat. Catal.* **2018**, *1* (7), 490–500. https://doi.org/10.1038/s41929-018-0092-7.

(14) Saadatjou, N.; Jafari, A.; Sahebdelfar, S. Ruthenium Nanocatalysts for Ammonia Synthesis: A Review. *Chem. Eng. Commun.* **2015**, *202* (4), 420–448. https://doi.org/10.1080/00986445.2014.923995.

(15) Shetty, S.; Jansen, A. P. J.; van Santen, R. A. Active Sites for N2 Dissociation on Ruthenium. *J. Phys. Chem. C* **2008**, *112* (46), 17768–17771. https://doi.org/10.1021/jp8085478.

(16) Rod, T. H.; Logadottir, A.; Nørskov, J. K. Ammonia Synthesis at Low Temperatures. *J. Chem. Phys.* **2000**, *112* (12), 5343–5347. https://doi.org/10.1063/1.481103.

(17) Murata, S.; Aika, K.-I. Preparation and Characterization of Chlorine-Free Ruthenium Catalysts and the Promoter Effect in Ammonia Synthesis: 1. An Alumina-Supported Ruthenium Catalyst. *J. Catal.* **1992**, *136* (1), 110–117. https://doi.org/10.1016/0021-9517(92)90110-4.

(18) Aika, K.; Takano, T.; Murata, S. Preparation and Characterization of Chlorine-Free Ruthenium Catalysts and the Promoter Effect in Ammonia Synthesis: 3. A Magnesia-Supported Ruthenium Catalyst. *J. Catal.* **1992**, *136* (1), 126–140. https://doi.org/10.1016/0021-9517(92)90112-U.

(19) Zhong, Z.; Aika, K. Effect of Ruthenium Precursor on Hydrogen-Treated Active Carbon Supported Ruthenium Catalysts for Ammonia Synthesis. *Inorganica Chim. Acta* **1998**, *280* (1), 183–188. https://doi.org/10.1016/S0020-1693(98)00202-3.

(20) Activated Chemisorption of Hydrogen on Supported Ruthenium: I. Influence of Adsorbed Chlorine on Accurate Surface Area Measurements. *J. Catal.* **1987**, *106* (1), 166–175. https://doi.org/10.1016/0021-9517(87)90221-1.

(21) Bécue, T.; Davis, R. J.; Garces, J. M. Effect of Cationic Promoters on the Kinetics of Ammonia Synthesis Catalyzed by Ruthenium Supported on Zeolite X. *J. Catal.* **1998**, *179* (1), 129–137. https://doi.org/10.1006/jcat.1998.2212.

(22) Larichev, Y. V.; Moroz, B. L.; Zaikovskii, V. I.; Yunusov, S. M.; Kalyuzhnaya, E. S.; Shur, V. B.; Bukhtiyarov, V. I. XPS and TEM Studies on the Role of the Support and Alkali Promoter in Ru/MgO and Ru−Cs+/MgO Catalysts for Ammonia Synthesis. *J. Phys. Chem. C* **2007**, *111* (26), 9427–9436. https://doi.org/10.1021/jp066970b.

(23) Fishel, C. T.; Davis, R. J.; Garces, J. M. Ammonia Synthesis Catalyzed by Ruthenium Supported on Basic Zeolites. *J. Catal.* **1996**, *163* (1), 148–157. https://doi.org/10.1006/jcat.1996.0314.

(24) Cisneros, M. D.; Lunsford, J. H. Characterization and Ammonia Synthesis Activity of Ruthenium Zeolite Catalysts. *J. Catal.* **1993**, *141* (1), 191–205. https://doi.org/10.1006/jcat.1993.1129.

(25) Kanbara, S.; Kitano, M.; Inoue, Y.; Yokoyama, T.; Hara, M.; Hosono, H. Mechanism Switching of Ammonia Synthesis Over Ru-Loaded Electride Catalyst at Metal–Insulator Transition. *J. Am. Chem. Soc.* **2015**, *137* (45), 14517–14524. https://doi.org/10.1021/jacs.5b10145.

(26) Niwa, Y.; Aika, K. The Effect of Lanthanide Oxides as a Support for Ruthenium Catalysts in Ammonia Synthesis. *J. Catal.* **1996**, *162* (1), 138–142. https://doi.org/10.1006/jcat.1996.0268.

(27) Wang, Z.; Liu, B.; Lin, J. Highly Effective Perovskite-Type BaZrO3 Supported Ru Catalyst for Ammonia Synthesis. *Appl. Catal. Gen.* **2013**, *458*, 130–136. https://doi.org/10.1016/j.apcata.2013.03.037.

(28) Zheng, J.; Liao, F.; Wu, S.; Jones, G.; Chen, T.; Fellowes, J.; Sudmeier, T.; McPherson, I. J.; Wilkinson, I.; Tsang, S. C. E. Efficient Non-dissociative Activation of Dinitrogen to Ammonia over Lithium-Promoted Ruthenium Nanoparticles at Low Pressure. *Angew. Chem. Int. Ed.* **2019**, *58* (48), 17335–17341. https://doi.org/10.1002/anie.201907171.

(29) Wang, P.; Chang, F.; Gao, W.; Guo, J.; Wu, G.; He, T.; Chen, P. Breaking Scaling Relations to Achieve Low-Temperature Ammonia Synthesis through LiH-Mediated Nitrogen Transfer and Hydrogenation. *Nat. Chem.* **2017**, *9* (1), 64–70. https://doi.org/10.1038/nchem.2595.

(30) Kitano, M.; Inoue, Y.; Yamazaki, Y.; Hayashi, F.; Kanbara, S.; Matsuishi, S.; Yokoyama, T.; Kim, S.-W.; Hara, M.; Hosono, H. Ammonia Synthesis Using a Stable Electride as an Electron Donor and Reversible Hydrogen Store. *Nat. Chem.* **2012**, *4* (11), 934–940. https://doi.org/10.1038/nchem.1476.

(31) Manabe, R.; Nakatsubo, H.; Gondo, A.; Murakami, K.; Ogo, S.; Tsuneki, H.; Ikeda, M.; Ishikawa, A.; Nakai, H.; Sekine, Y. Electrocatalytic Synthesis of Ammonia by Surface Proton Hopping. *Chem. Sci.* **2017**, *8* (8), 5434–5439. https://doi.org/10.1039/C7SC00840F.

(32) Kochetova, N.; Animitsa, I.; Medvedev, D.; Demin, A.; Tsiakaras, P. Recent Activity in the Development of Proton-Conducting Oxides for High-Temperature Applications. *RSC Adv.* **2016**, *6* (77), 73222–73268. https://doi.org/10.1039/C6RA13347A.

(33) Yamazaki, Y.; Blanc, F.; Okuyama, Y.; Buannic, L.; Lucio-Vega, J. C.; Grey, C. P.; Haile, S. M. Proton Trapping in Yttrium-Doped Barium Zirconate. *Nat. Mater.* **2013**, *12* (7), 647–651. https://doi.org/10.1038/nmat3638.

(34) Iwahara, H.; Esaka, T.; Uchida, H.; Maeda, N. Proton Conduction in Sintered Oxides and Its Application to Steam Electrolysis for Hydrogen Production. *Solid State Ion.* **1981**, *3–4*, 359–363. https://doi.org/10.1016/0167-2738(81)90113-2.

(35) Yamazaki, Y.; Hernandez-Sanchez, R.; Haile, S. M. High Total Proton Conductivity in Large-Grained Yttrium-Doped Barium Zirconate. *Chem. Mater.* **2009**, *21* (13), 2755–2762. https://doi.org/10.1021/cm900208w.

(36) Fabbri, E.; Bi, L.; Pergolesi, D.; Traversa, E. Towards the Next Generation of Solid Oxide Fuel Cells Operating Below 600 °C with Chemically Stable Proton-Conducting Electrolytes. *Adv. Mater.* **2012**, *24* (2), 195–208. https://doi.org/10.1002/adma.201103102.

(37) Yamazaki, Y.; Blanc, F.; Okuyama, Y.; Buannic, L.; Lucio-Vega, J. C.; Grey, C. P.; Haile, S. M. Proton Trapping in Yttrium-Doped Barium Zirconate. *Nat. Mater.* **2013**, *12* (7), 647–651. https://doi.org/10.1038/nmat3638.

(38) Kreuer, K. D.; Münch, W.; Traub, U.; Maier, J. On Proton Transport in Perovskite-Type Oxides and Plastic Hydroxides. *Berichte Bunsenges. Für Phys. Chem.* **1998**, *102* (3), 552–559. https://doi.org/10.1002/bbpc.19981020339.

(39) Kreuer, K. d. Proton-Conducting Oxides. *Annu. Rev. Mater. Res.* **2003**, *33* (1), 333–359. https://doi.org/10.1146/annurev.matsci.33.022802.091825.

(40) Han, D.; Hatada, N.; Uda, T. Chemical Expansion of Yttrium-Doped Barium Zirconate and Correlation with Proton Concentration and Conductivity. *J. Am. Ceram. Soc.* **2016**, *99* (11), 3745–3753. https://doi.org/10.1111/jace.14377.

(41) Han, D.; Hatada, N.; Uda, T. Microstructure, Proton Concentration and Proton Conductivity of Barium Zirconate Doped with Ho, Er, Tm and Yb. *J. Electrochem. Soc.* **2016**, *163* (6), F470–F476. https://doi.org/10.1149/2.0551606jes.

(42) Malavasi, L.; Fisher, C. A. J.; Islam, M. S. Oxide-Ion and Proton Conducting Electrolyte Materials for Clean Energy Applications: Structural and Mechanistic Features. *Chem. Soc. Rev.* **2010**, *39* (11), 4370–4387. https://doi.org/10.1039/B915141A.

(43) Nyman, B. J. Proton Conductivity of Lanthanum and Barium Zirconate: Microscale Aspects on First-Principles Basis. Doctoral thesis, Chalmers University of Technology, 2012.

(44) Iwahara, H.; Yajima, T.; Hibino, T.; Ozaki, K.; Suzuki, H. Protonic Conduction in Calcium, Strontium and Barium Zirconates. *Solid State Ion.* **1993**, *61* (1), 65–69. https://doi.org/10.1016/0167-2738(93)90335-Z.

(45) Hibino, T.; Mizutani, K.; Yajima, T.; Iwahara, H. Characterization of Proton in Y-Doped SrZrO3 Polycrystal by IR Spectroscopy. *Solid State Ion.* **1992**, *58* (1), 85–88. https://doi.org/10.1016/0167-2738(92)90014-G.

(46) Cukierman, S. Et Tu, Grotthuss! And Other Unfinished Stories. *Biochim. Biophys. Acta BBA - Bioenerg.* **2006**, *1757* (8), 876–885. https://doi.org/10.1016/j.bbabio.2005.12.001.

(47) Kreuer, K.-D.; Fuchs, A.; Maier, J. HD Isotope Effect of Proton Conductivity and Proton Conduction Mechanism in Oxides. *Solid State Ion.* **1995**, *77*, 157–162. https://doi.org/10.1016/0167-2738(94)00265-T.

(48) Kreuer, K. D. Aspects of the Formation and Mobility of Protonic Charge Carriers and the Stability of Perovskite-Type Oxides. *Solid State Ion.* **1999**, *125* (1), 285–302. https://doi.org/10.1016/S0167-2738(99)00188-5.

(49) Braun, A.; Chen, Q. Experimental Neutron Scattering Evidence for Proton Polaron in Hydrated Metal Oxide Proton Conductors. *Nat. Commun.* **2017**, *8* (1), 15830. https://doi.org/10.1038/ncomms15830.

(50) Kawaguchi, S.; Takemoto, M.; Osaka, K.; Nishibori, E.; Moriyoshi, C.; Kubota, Y.; Kuroiwa, Y.; Sugimoto, K. High-Throughput Powder Diffraction Measurement System Consisting of Multiple MYTHEN Detectors at Beamline BL02B2 of SPring-8. *Rev. Sci. Instrum.* **2017**, *88* (8), 085111. https://doi.org/10.1063/1.4999454.

(51) Morgan, D. J. Resolving Ruthenium: XPS Studies of Common Ruthenium Materials. *Surf. Interface Anal.* **2015**, *47* (11), 1072–1079. https://doi.org/10.1002/sia.5852.

(52) Yang, B. X.; Kirz, J. Soft X-Ray Absorption Cross Section of Argon Determined by a Variable Absorber Technique. *Appl. Opt.* **1987**, *26* (18), 3823–3826. https://doi.org/10.1364/AO.26.003823.

(53) Jablonski, A.; Salvat, F.; Powell, C. J.; Lee, A. Y. *NIST Electron Elastic-Scattering Cross-Section Database Version 4.0*; NIST Standard Reference Database Number 64; National Institute of Standards and Technology, 2006.

(54) Han, D.; Shinoda, K.; Sato, S.; Majima, M.; Uda, T. Correlation between Electroconductive and Structural Properties of Proton Conductive Acceptor-Doped Barium Zirconate. *J. Mater. Chem. A* **2014**, *3* (3), 1243–1250. https://doi.org/10.1039/C4TA05701E.

(55) Rajesh, T.; Devi, R. N. Role of Oxygen Vacancies in Water Gas Shift Reaction: Activity Study on BaCe0.98–XYxPt0.02O3−δ Perovskites. *J. Phys. Chem. C* **2014**, *118* (36), 20867–20874. https://doi.org/10.1021/jp503922x.

(56) Mburu, C. W.; Gaita, S. M.; Knee, C. S.; Gatari, M. J.; Karlsson, M. Influence of Yttrium Concentration on Local Structure in BaZr1–XYxO3−δ Based Proton Conductors. *J. Phys. Chem. C* **2017**, *121* (30), 16174–16181. https://doi.org/10.1021/acs.jpcc.7b05023.

(57) Shimoda, N.; Kimura, Y.; Kobayashi, Y.; Kubota, J.; Satokawa, S. Ammonia Synthesis over Yttrium-Doped Barium Zirconate and Cerate-Based Perovskite-Type Oxide Supported Ruthenium Catalysts. *Int. J. Hydrog. Energy* **2017**, *42* (50), 29745–29755. https://doi.org/10.1016/j.ijhydene.2017.10.108.

(58) Ding, J.; Balachandran, J.; Sang, X.; Guo, W.; Anchell, J. S.; Veith, G. M.; Bridges, C. A.; Cheng, Y.; Rouleau, C. M.; Poplawsky, J. D.; Bassiri-Gharb, N.; Unocic, R. R.; Ganesh, P. The Influence of Local Distortions on Proton Mobility in Acceptor Doped Perovskites. *Chem. Mater.* **2018**, *30* (15), 4919–4925. https://doi.org/10.1021/acs.chemmater.8b00502.

(59) Kitano, M.; Inoue, Y.; Sasase, M.; Kishida, K.; Kobayashi, Y.; Nishiyama, K.; Tada, T.; Kawamura, S.; Yokoyama, T.; Hara, M.; Hosono, H. Self-Organized Ruthenium–Barium Core–Shell Nanoparticles on a Mesoporous Calcium Amide Matrix for Efficient Low-Temperature Ammonia Synthesis. *Angew. Chem.* **2018**, *130* (10), 2678–2682. https://doi.org/10.1002/ange.201712398.

(60) Ogura, Y.; Sato, K.; Miyahara, S.; Kawano, Y.; Toriyama, T.; Yamamoto, T.; Matsumura, S.; Hosokawa, S.; Nagaoka, K. Efficient Ammonia Synthesis over a Ru/La 0.5 Ce 0.5 O 1.75 Catalyst Pre-Reduced at High Temperature. *Chem. Sci.* **2018**, *9* (8), 2230–2237. https://doi.org/10.1039/C7SC05343F.

(61) Shimoda, N.; Kimura, Y.; Kobayashi, Y.; Kubota, J.; Satokawa, S. Ammonia Synthesis over Yttrium-Doped Barium Zirconate and Cerate-Based Perovskite-Type Oxide Supported Ruthenium Catalysts. *Int. J. Hydrog. Energy* **2017**, *42* (50), 29745–29755. https://doi.org/10.1016/j.ijhydene.2017.10.108.

(62) Wu, S.; Peng, Y.-K.; Chen, T.-Y.; Mo, J.; Large, A.; McPherson, I.; Chou, H.-L.; Wilkinson, I.; Venturini, F.; Grinter, D.; Ferrer Escorihuela, P.; Held, G.; Tsang, S. C. E. Removal of Hydrogen Poisoning by Electrostatically Polar MgO Support for Low-Pressure NH3 Synthesis at a High Rate over the Ru Catalyst. *ACS Catal.* **2020**, *10* (10), 5614–5622. https://doi.org/10.1021/acscatal.0c00954.

(63) Rosowski, F.; Hornung, A.; Hinrichsen, O.; Herein, D.; Muhler, M.; Ertl, G. Ruthenium Catalysts for Ammonia Synthesis at High Pressures: Preparation, Characterization, and Power-Law Kinetics. *Appl. Catal. Gen.* **1997**, *151* (2), 443–460. https://doi.org/10.1016/S0926-860X(96)00304-3.

(64) Ozaki A.; Taylor Hugh Stott; Boudart M. Kinetics and Mechanism of the Ammonia Synthesis. *Proc. R. Soc. Lond. Ser. Math. Phys. Sci.* **1960**, *258* (1292), 47–62. https://doi.org/10.1098/rspa.1960.0174.

(65) Han, D.; Shinoda, K.; Tsukimoto, S.; Takeuchi, H.; Hiraiwa, C.; Majima, M.; Uda, T. Origins of Structural and Electrochemical Influence on Y-Doped BaZrO3 Heat-Treated with NiO Additive. *J. Mater. Chem. A* **2014**, *2* (31), 12552–12560. https://doi.org/10.1039/C4TA01689K.

(66) Sata, N.; Hiramoto, K.; Ishigame, M.; Hosoya, S.; Niimura, N.; Shin, S. Site Identification of Protons in ${\mathrm{SrTiO}}_{3}$: Mechanism for Large Protonic Conduction. *Phys. Rev. B* **1996**, *54* (22), 15795–15799. https://doi.org/10.1103/PhysRevB.54.15795.

(67) Kinyanjui, F. G.; Norberg, S. T.; Knee, C. S.; Ahmed, I.; Hull, S.; Buannic, L.; Hung, I.; Gan, Z.; Blanc, F.; Grey, C. P.; Eriksson, S. G. Crystal Structure and Proton Conductivity of BaSn0.6Sc0.4O3−δ: Insights from Neutron Powder Diffraction and Solid-State NMR Spectroscopy. *J. Mater. Chem. A* **2016**, *4* (14), 5088–5101. https://doi.org/10.1039/C5TA09744D.

(68) Buannic, L.; Sperrin, L.; Dervişoğlu, R.; Blanc, F.; Grey, C. P. Proton Distribution in Sc-Doped BaZrO3: A Solid State NMR and First Principle Calculations Analysis. *Phys. Chem. Chem. Phys.* **2018**, *20* (6), 4317–4328. https://doi.org/10.1039/C7CP08523K.

(69) Ito, T.; Nagasaki, T.; Iwasaki, K.; Yoshino, M.; Matsui, T.; Igawa, N.; Ishii, Y. Location of Deuterium Atoms in BaSn0.5In0.5O2.75+α by Neutron Powder Diffraction at 10 K. *Solid State Ion.* **2007**, *178* (1), 13–17. https://doi.org/10.1016/j.ssi.2006.10.030.

TOC Graphic